TECHNISCHE UNIVERSITÄT DRESDEN

Faculty of Computer Science Institute of Artificial Intelligence

DYNAMIC THERMAL IMAGING FOR INTRAOPERATIVE MONITORING OF NEURONAL ACTIVITY AND CORTICAL PERFUSION

Dipl.-Inf. Nico Hoffmann
Born on: 26.2.1987 in Pirna

DISSERTATION (EXTENDED ABSTRACT)

to achieve the academic degree

DOKTOR RERUM NATURALIUM (DR. RER. NAT.)

Supervisor
Sen.-Prof. Dr.-Ing. habil. Uwe Petersohn

Dresden, April 2016

1 INTRAOPERATIVE THERMAL NEUROIMAGING

Thermal imaging (TI) is an imaging technique that detects the emitted heat radiation of a target object and converts it into temperature values. Heat propagates through various layers of an object, making inner heat sources visible at outer layers or even at the surface. In the present work, we will discuss the application of this technique to intraoperative neuroimaging to analyse human tissue.
Pathological changes of the central nervous system (CNS) require medical intervention in the field of neurosurgery. Latter is a highly specialized and technological medical discipline covering the diagnostics and treatment of disorders of the CNS. For diagnostics and OP planning, a close collaboration with neuroradiology is necessary, since this discipline provides necessary imaging tools and experience for reasoning about neurological disorders. Hereby, neuroimaging denotes various approaches to measure and visualize functional and structural information at different scales.

1.1 BRAIN TUMOUR

The steady growth of abnormal cells in the brain is called brain tumour. These cells can be categorized by their origin, for example Glioblastoma multiforme originate from a massive proliferation of Glial cells. This growth increases intracerebral pressure (ICP) causing patho-physiological symptoms like oedema [17]. ICP induced by brain tumour causes severe tissue mass movements, a compression of the brainstem as well as a displacement of parts of the temporal lobe into the posterior cranial fossa [17]. These consequence significantly endanger the patient's life. Approximately 6,920 Germans develop a primary brain tumour every year [15]. In the same year, 5,646 cases of death were reported[15].

1.2 ISCHAEMIC STROKE

Stroke denotes the shortage of substrates like glucose in delimited parts of the brain. This shortage may be caused by embolic or thrombotic blockage (ischaemic stroke) of a vessel. Both lead to a (potentially irreversible) loss of brain function of the affected tissue depending

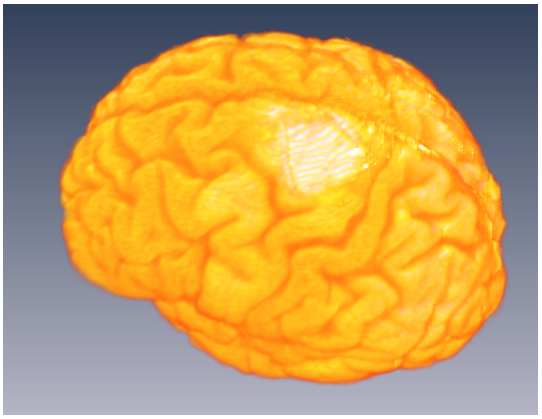

(a) Cortex reconstruction from preoperative MRI of a intracranial tumour.

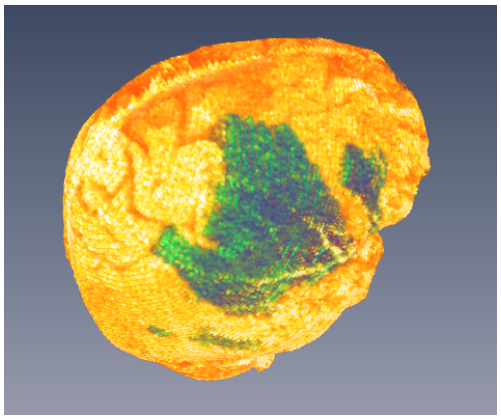

(b) Cortex reconstruction with ischaemic demarcation shown in green.

Figure 1.1: **(a)** The white cluster in this image resembles the contrast enhancement of a grade III Oligoastrocytoma on precentral gyrus. **(b)** shows the 3d cortex reconstruction of a patient undergoing MCA occlusion. The infarct demarcation is segmented as green area.

on the duration of the shortage. As consequence, a chain of biochemical reactions to hypoperfusion is initiated leading to loss of function, cell death and forming of a cerebral oedema. When the shortage is below some threshold structure metabolism can't be maintained properly causing pathological changes of tissue [17]. A shortage of oxygen and glucose for 60 *s* to 90 *s* causes neurons to pause functional activity. Irreversible damage is induced after a nutrition shortage of about 3 *h*. In 2008, 196,000 Germans suffered from a first-time stroke with 63,000 cases of death [8]. Latter makes a stroke the third most cause of death in Germany right after heart diseases and cancer.

1.3 THESIS CONTRIBUTION

Intraoperative thermal neuroimaging is used to measure the emitted heat radiation of the cerebral cortex which allows to draw conclusions regarding cortical perfusion. We enrich these information by an efficient 2D - 3D image fusion framework to combine preoperative structural information from volumetric MRI recordings with intraoperative thermal neuroimaging data. The quality of thermal imaging data is further improved by filtering camera motion based on the recognition of characteristic patterns in time-frequency domain. Based on these findings we developed a FPGA-based motion correction scheme resting upon hardware optical flow estimation. These building blocks now enable us to quantify cortical perfusion in a standardized way using a machine learning framework that detects cortical rinsings at minimal delay. This framework is employed for intraoperative classification of the cortical perfusion state in case of ischaemic strokes. Latter might enable novel research regarding the prediction of infarct demarcations and potential future intraoperative therapies for hypoperfused tissue. Perfusion changes induced by neurovascular coupling also allow neural activity monitoring. We propose a semiparametric regression framework that incorporates experimental conditions (like nerve stimulations) and non-deterministic random artefacts that are

specific to thermal imaging devices. This approach allows us to unveil and visualize neural activity of the primary somatosensory cortex and provides surgeons a tool to differentiate functionally active tissue from tumour tissue. In case of tumour resections, this information is important to predict and minimize potential post-operative functional deficits and preserve the patient's quality of living as long as possible.

2 IMPROVING PREDICTIVE ACCURACY AND PERFORMANCE OF THERMAL NEUROIMAGING

This chapter discusses novel aspects for improved quality, signal to noise ratio and visualization of intraoperative thermal imaging data. A feature representation scheme that allows foreground-background segmentation is discussed in section 2.1. This approach depicts a basic building block towards learning representations of thermal data to discriminate tissue state based on intrinsic thermal properties. Since thermographic images contain weakly differentiated anatomic information and are prone to artefacts originating from physiological and environmental sources, further data correction methods are required. In section 2.2, approaches to the estimation and correction of motion artefacts are discussed. We also propose an efficient FPGA-based hardware motion correction scheme in section 2.3 allowing online correction of motion artefacts. Thermal neuroimaging systems measure the emitted heat of the exposed cerebral cortex, which in turn is mainly influenced by tissue perfusion. This hampers the visual matching of specific area of thermal images with other modalities like intraoperative optical imaging or preoperative MR or CT imaging. We approach this challenge by a generic image registration and image fusion framework in section 2.4. Multimodal image fusion further allows the surgeon to better assess the quality of the gained results and depicts an important foundation stone to integration of anatomical and morphological information into data analytics to quantify functional connectivity, detect focal epileptic sites or for improved tissue differentiation.

2.1 LEARNING THERMAL PROCESS REPRESENTATIONS FOR CLASSIFICATION OF CEREBRAL CORTEX

Intraoperative imaging imposes several changes to the employed algorithms. One such is to minimize the intraoperative delay. This constraint can be approached by restricting the analysis to foreground objects. For this purpose we note that the thermic time-behaviour of the exposed cerebral cortex is influenced by artificial noise sources like baseline drift of the thermographic signal. Cortical perfusion further contributes to the overall thermic signal, yet the actual influence to the measured thermographic signal is not fully understood yet. To

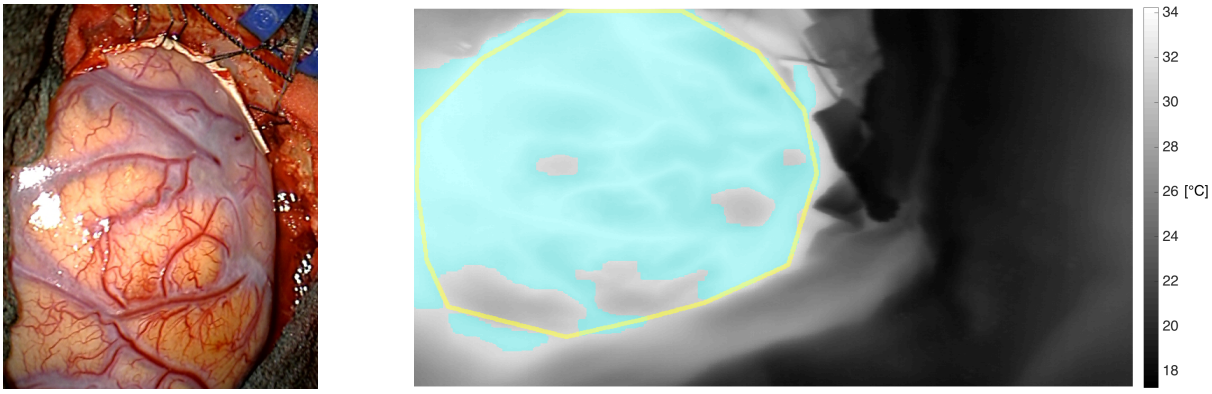

(a) (b)

Figure 2.1: Thermal neuroimaging is typically done just after exposure of the cerebral cortex as shown in **(a)**. This recording was then subject to the AE-CRF classifier and the results are shown in **(b)**. Expert classification of the cerebral cortex is indicated by the yellow solid line and the classification result is shown in turquoise.

approach this issue an unsupervised autoencoder is trained to learn latent thermic representations of the cortex' dynamic temporal behaviour[12]. The probability distribution of these high-level features is then learnt by a random forest. The regular and neighbourhood structure of the imaging data is further exploited by integrating the local probabilities in a conditional random field with pairwise Potts model potentials. Summarizing, the framework learns characteristic thermodynamic features which are afterwards employed to classify intraoperative thermal recordings.

Prior to recovering a representation we have to estimate and remove the smooth background signal $T^{bg} = B_{2d}\widehat{\alpha}$ first by regressing $vec(T) = B_{2d}\alpha$ using least squares:

$$\widehat{\alpha} = (B_{2d}^T B_{2d})^{-1} B_{2d}^T vec(T) \tag{2.1}$$

with column stacked version $vec(T) \in \mathcal{R}^{nm}$ of the thermal data T and the tensor product $B_{2d} = B_{xy} \otimes B_t$ of two 1D B-Spline bases (see [4] for details). High-level features $f(c_i)$ are now learnt from the background corrected and wavelet transformed signal $c_i(j, k)$ of pixel i at scale j and point k given some wavelet function ϕ

$$c_i(j, k) = \sum_j \sum_k (T_i(k) - T_i^{bg}(k)) 2^{-j/2} \phi(2^{-j} n - k) \tag{2.2}$$

with an linear autoencoder[22] (AE). This AE consists of an encoding $f(c_i)$ and decoding function $g(f(c_i))$ so that $(g \circ f)(c_i) = AE(c_i) \approx c_i$. The functions g,f are commonly modelled as sigmoid function with weight matrix $W \in \mathcal{R}^{d' \times m}$, bias vector $x \in \mathcal{R}^{d'}$. The decoding function $g(x)$ is constructed by a tied weight $W' = W^T$:

$$f(c_i) = sigm(W c_i + b) \tag{2.3}$$

$$g(c_i) = sigm(W' c_i + b') \tag{2.4}$$

It has to be noted that the output of $f(c_i)$ is a lower-dimensional $d' \ll m$ compact representation of c_i meaning that the decoder $g(f(c_i))$ has to reconstruct the higher-dimensional c_i from a

lower-dimensional projection $f(c_i)$. This approach preserves information while dropping noise terms. Recent developments aim to stack multiple AEs and train each layer independently[1]. The learning task is to minimize the reconstruction error of the input data whilst sparsity constraints are imposed to prevent overfitting[22]. Commonly, this learning is realized by minimizing a penalized squared loss function.
The probability distribution $p_i(y_i|f(c_i))$ of the unveiled high-level features for pixel i is then learnt by a bagged random forest given a bootstrap sampled training set $(f(c_i), y_i)$ of $1 \leq i \leq n_t$ elements and labels $y_i \in \mathcal{Y}$ with $\mathcal{Y} = \{fg, bg\}$. In our case $p_i(y_i|f(c_i))$ represents the (un-)certainty that the encoded signal $f(c_i)$ belongs to state foreground $p(y_i = fg|f(c_i))$ or background $p(y_i = bg|f(c_i))$. By exploiting the intrinsic regular structure of imaging data by a conditional random field we further improve the overall accuracy. A discriminative CRF model allows us to infer a global consistent state z_i depending only on the local probability $p_i(y_i)$ and of a probability distribution $p(z_f|y_f)$ factored given the neighbour's $f \in \mathcal{N}_i$ of pixel i. In general, the posterior distribution $p(Y|\mathcal{F}_\mathcal{C})$ of latent variables $y_i \in \mathcal{Y}$ and observations $f(c_i) \in \mathcal{F}_\mathcal{C}$ can be formulated in terms of unary Ψ and pairwise terms Φ on a undirected graph $G = (V, E)$ as of

$$log\ p(Y|\mathcal{F}_\mathcal{C}) = \sum_{i \in V} \Psi_i(y_i, f(c_i)) + \sum_{(i,i') \in E} \Phi(y_i, y_{i'}, f(c_i), f(c_{i'})) \tag{2.5}$$

Note that since only adjacent pixels i, i' are connected by an edge in E efficient factoring of equation 2.5 and therefore fast inference is achieved. The unary potential encodes the prior probability learnt by the RF classifier whilst the pairwise potential encodes structural information. To simplify computations and exploit the structure of the imaged data we employ a Potts model:

$$\Phi(y_i, y_{i'}, f(c_i), f(c_{i'}) = C \cdot 1_{y_t = y_{t'}} \tag{2.6}$$

with indicator function 1 and C being a smoothness penalty. Since we are dealing with binary labels and Potts model equation 2.5 is submodular allowing the application of very efficient inference method based on graph cuts. Minimizing equation 2.5 now corresponds to finding a maximum a-posteriori estimate for the labelling Y.

We found that introducing these latent feature representations yielded significant perfor-

RF accuracy [%]	μT	BoW	PCA	AE	SAE
test	81.1	92.8	**96.5**	95.5	92.1
validation	81.1	87.4	**88**	87.3	85.1

Table 2.1: Using a single Random Forest classifier, there is a clear gain in accuracy by the application of learnt high-level dynamic thermal features.

mance improvements compared to a only temperature-based model for segmentation of foreground to background pixels. The results indicate that thermodynamic parameters of cortical tissue allow more fine-grain reasoning about tissue. This approach might be a first step towards fine-grained tissue characterization by means of its dynamic temperature behaviour. In contrary to classical machine learning approaches, no explicit feature crafting is required since discriminative features are learnt independently. Therefore, the framework is not limited to the discussed segmentation task but introduces enough flexibility to unveil various pathological patterns, if these can be characterized by thermal behaviour.

CRF accuracy [%]	μT	BoW	PCA	AE	SAE
test	86.1	94.4	**98.5**	98	94.8
validation	87.7	89.1	88.8	**89.2**	88

Table 2.2: The RF-CRF model compensates false negatives of the plain RF classifier and improved its performance considerably.

2.2 FILTERING OF CAMERA MOVEMENT ARTEFACTS

Intraoperative recordings of thermal imaging systems require object distances below 30cm to minimize the influence of external noise sources. For this purpose, the camera is mounted at the operating table by a system consisting of several freely moveable hinges. This camera setup is prone to vibrations, for example caused by the initial orientation of the camera or during electrical stimulations. These induce a periodic shift of the whole camera introducing artefacts into the time course of each pixel. In case of weak signal to noise ratio, the induced motion artefact might superimpose existing signals at same frequency range. We solve this challenge by detecting and removing characteristic components in time-frequency domain that originate from global camera motion[9]. The camera movement leads to a linear shift of all pixels in the same direction at small time scales. Therefore, all pixels follow the same trajectory and show similar behaviour. The amplitude of the error strongly depends on the pixels Jacobian matrix. High values and therefore distinct gradients induce strong artefacts.
Let the time course of n pixels be modelled by $X_{raw} \in \mathbb{R}^{n \times m}$ with $m = 2^{j_{max}+1}$ and $j_{max} \in \mathbb{N}^+$. Let further denote $X^j \in \mathbb{R}^{n \times m}$ the wavelet transformed X_{raw} (see the previous section) at wavelet scale j. Various components superimpose the data in this domain, for example periodic heart rate patterns, neural activity and global motion artefacts. One approach to differentiate latter artefacts from actual data is principal component analysis. PCA requires a eigenvalue decomposition of the empiric covariance matrices of the wavelet coefficients $X^j \in \mathbb{R}^{n \times 2^j}$ at wavelet scales $1 \leq j \leq j_{max}$. Each of the $1 \leq k \leq 2^j$ eigenvectors v_k^j describes a characteristic frequency pattern. By a change of basis of X^j given $\Phi = [v_1^j \cdots v_{2^j}^j]$ into

$$W^j = X^j \Phi = \begin{bmatrix} w_1(1) & \dots & w_{2^j}(1) \\ \vdots & \vdots & \vdots \\ w_{2^j}(n) & \dots & w_{2^j}(n) \end{bmatrix}$$

we represent all pixel's wavelet coefficients at scale j in terms of the eigenvectors v_k^j and score w_k. Eigenvector k describes a global time-frequency pattern that contributes to the overall time-frequency content of pixel i by $w_k(i) \in \mathbb{R}$.
Now we can form two sets of pixels. One containing pixels in distinct $\mathcal{X}^+$ and another containing pixels in a rather smooth $\mathcal{X}^-$ neighbourhoods. Distinct neighbourhoods lead to larger amplitudes of the error pattern compared to the expected strength of the artefacts in smooth neighbourhoods. We quantify this assumption by the subspace contribution ratio r_k (see figure 2.2):

$$r_k = w_k(\mathcal{X}^+) \,/\, w_k(\mathcal{X}^-) \tag{2.7}$$

Eigenvectors that resemble global motion artefacts lead to a skewed ratio of $w_k(\mathcal{X}^+)$ to $w_k(\mathcal{X}^-)$ hence cause significantly deviating values of r_k. In order to isolate these eigenvectors, we form a global motion impact factor $R^j = (r_1, r_2, ..., r_2^j)$ for each scale j. This factor is

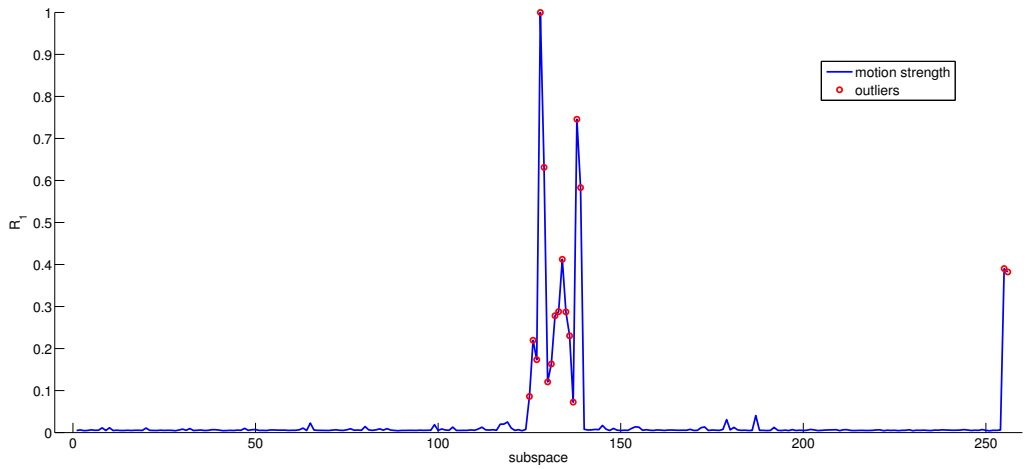

Figure 2.2: The subspace contribution ratio is modelled to take significantly outlying values in case of motion artefact specific components in time-frequency domain.

modelled as Gaussian random variable: $R \sim N(ax + b, \sigma)$. The parameters are fitted using iteratively-reweighted least squares and outlying r_j's are found by a t-Test with Bonferroni corrected significance level $\alpha = 0.05/m$ and m being the number of tests (pixels). Eigenvectors with outlying r_j's are then wiped and the motion corrected estimate is achieved by inverse PCA and inverse discrete wavelet transform.
This procedure was applied to representative intraoperative imaging data. We used average spectral density as accuracy metric since no groundtruth information is available. Dataset 1 was recorded during an ECoG measurement consisting of high-frequent vibrations of the camera system at a spatial extent of 5 pixels ($\sim$ 1cm). After application of the proposed method any motion artefact visually disappeared. The average spectral density was further significantly lowered by the proposed method. The second dataset consists of weak motion artefacts at strong spatially varying thermic background noise. Even in this case, the average spectral density was highly reduced and any motion visually disappeared. Using the discussed motion correction scheme, we are able to estimate the actual error pattern and integrate it into subsequent data analysis workflows. It further allows us to differentiate global artefacts from local periodic effects with similar spectral bandwidth. Latter is especially useful since it is now able to differentiate motion terms from pulse-rate frequency components.

2.3 OBJECT-BASED MOTION CORRECTION BY HARDWARE OPTICAL FLOW ESTIMATION

Based on the promising results of the just discussed approach we will now discuss our extension towards online motion correction[19], [20]. Online methods are a favourable extension since they do not introduce further delay to intraoperative workflows. The approach bases on estimating object-based optical flow between adjacent frames on FPGA hardware using cellular non-linear networks.

The translation $(\Delta x, \Delta y)$ of a pixel is modelled given

$$(I(x, y, t+1) - I(x, y, t)) \approx \frac{\delta I}{\delta x}\Delta x + \frac{\delta I}{\delta y}\Delta y \tag{2.8}$$

Object-based optical flow estimation requires a slight modification to former equation yet yields an algorithm being more robust to noise. Suppose global motion has occurred and we are given pixels $k_i \in W$ with $1 \leq i \leq N$ of an arbitrary partition $k \in X$ of the set X of pixels. Solving the basic equation of object-based optical flow estimation (equation 2.9) using least squares now yields an estimate for global motion in Δx and Δy direction within time points t and $t + 1$:

$$\begin{bmatrix} K(t; w_1) \\ \vdots \\ K(t; w_4) \end{bmatrix} = \begin{bmatrix} K_{X1}(t) & K_{Y1}(t) \\ \vdots & \vdots \\ K_{X4}(t) & K_{Y4}(t) \end{bmatrix} \begin{bmatrix} \Delta x \\ \Delta y \end{bmatrix} \tag{2.9}$$

given 4 windows, $K(t; w) = \sum_{p \in w} I_p(t+1) - I_p(t)$ and K_{X_j}, K_{Y_j} being the summed partial derivates of window j.
The approach was implemented on a novel CNN FPGA hardware platform for high-speed signal processing[2]. The approach was applied to intraoperative data and compared to the just discussed PCA-based method. Run times of 4.7 ms (8Bit) and 13.3 ms (12 Bit) per frame validate the demanded online performance since the thermal imaging system records data at 50 Hz. The evaluation yielded results with accuracy being comparable to the offline PCA-based method. We found that for larger cortex images an improved window selection scheme must be employed. In summary the approach is an efficient and generic scheme for hardware optical flow estimation and motion correction which is applicable to thermal imaging data recorded during arbitrary neurosurgical interventions.

2.4 IMAGE FUSION OF INTRAOPERATIVE THERMAL IMAGING WITH PREOPERATIVE MRI

Thermal images originate from the emitted heat of a body leading to smooth images without distinct gradients. This hampers the exact correlation with structural (anatomic) features to some extent. In order to combine information recovered from analysing the heat distribution with structural features, image registration of the imaging modalities must be done. We approach this idea by a generic 2D-3D calibration based image registration and image fusion framework[14].
Guided tumour resections are typically supported by intraoperative Neuronavigation systems. These systems require the registration of the patient with preoperative imaging modalities by matching the position of so called fiducial markers in preoperative datasets and during op. It is further possible to track the spatial position of a so called instrument adapter, which in turn can be attached to arbitrary devices. By exploiting this fact, the main task of the developed framework is to establish a projection of the spatial position of the instrument adapter to the position of the sensor array of the imaging device in MRI coordinate space. The following compound affine transformation T maps the spatial position of the instrument adapter onto the position of the imaging system's sensor array and corrects the dimensions of the virtual image plane:

$$T = M_{\text{scale}} * M_c * M_a * M_{\text{Brainlab}} \tag{2.10}$$

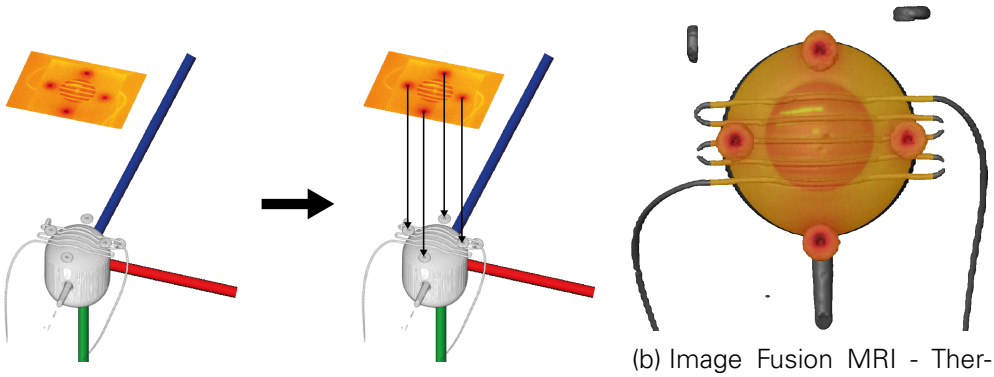

(a) Orthogonal Projection

(b) Image Fusion MRI - Thermography

Figure 2.3: By using an orthogonal projection as seen in (a), it is possible to map 2D planes onto 3D surfaces (b).

given camera calibration matrix M_c, additional transformations M_a, the spatial position and orientation of the instrument adapter M_{Brainlab} and virtual pixel size correction denoted by M_{scale}. The parameters are estimated once by an offline calibration scheme. Subsequent image fusion is realized by an orthogonal projection that maps 2D coordinates onto the nearest coordinate in MRI coordinate system (see figure 2.3).

Our experiments were realized using a novel imaging phantom[23] which was recorded by a 3D MRI Siemens Magnetom Verio scanner. Accuracy analysis was done by an exhaustive evaluation suite to quantify influence factors like calibration of the instrument adapter, tracking beam accuracy, MRI accuracy, orientation of the camera wrt. the surface. We identified that the mounting of the instrument adapter affects the overall system accuracy the most. In order to estimate the worst-case accuracy, we placed the IA at extremal positions and measured a worst-case inaccuracy of 1 cm. In thermal imaging this would be a uncertainty of about 5 pixel. The average accuracy of the system is 2.46 mm.

In [10] we proposed a segmentation algorithm to isolate vessel structures in thermal imaging data by their characteristic thermal behaviour. In combination with recovering such structures in optical imaging data, feature-based co-registration of both modalities might be achievable so that the discussed 2D-3D framework is not limited to a single intraoperative 2D imaging device. Given the achieved accuracy, the discussed image fusion framework enables the intraoperative multimodal image fusion, so that extracted information from 2D intraoperative imaging devices like thermal- or optical imaging can be combined with and integrated into intraoperative neuronavigation systems. This allows the surgeon to validate the gained results by means their anatomic localization as well as to combine rather abstract thermal information with morphological structures. Another future approach depicts the extraction of anatomic and tissue information from preoperative 3D imaging like CTI or MRI for their integration as prior into data analytics frameworks. The influence of vascular disease to the arrival time of intraoperative arrival time of perfusion tracers could now be modelled by exploiting structures from preoperative magnetic resonance angiography recordings. Another future aspect might be the utilization of specific information from human brain atlases, like the localization of Broadman areas relative to the exposed cerebral cortex, for analysis of neural activity in order to improve statistical hypothesis testing.

3 TIME-RESOLVED THERMOGRAPHY FOR TISSUE PERFUSION ANALYSIS IN NEUROSURGERY

Active dynamic thermography denotes the method of applying temperature gradients to an object in order to analyse its time-dependent thermal behaviour. In medical thermal imaging, this method was used for analysis of burned skin[16], tumour tissue[7] and cortical perfusion[21]. We extend these findings by seamless intraoperative workflow in combination with a generic mathematical framework for detection of NaCl rinsings of the cortex surface and subsequent standardization and classification of cortical perfusion[11]. This framework is applied to the analysis of tissue perfusion of cases with ischemia. We propose to evaluate the heat distribution of the exposed cortex after application of a cold NaCl solution to the surface.

3.1 RINSING DETECTION AND CLASSIFICATION FRAMEWORK

Cortical rinsings are a common method in neurosurgery as they prevent dehydration of exposed tissue and therefore don't impose any harm to the patient or require special tools. All rinsing events were detected and candidate selection for subsequent heating analysis is achieved by a novel machine learning detection framework. The main idea is to partition the data into overlapping windows and recognize learnt characteristic rinsing features (see fig-

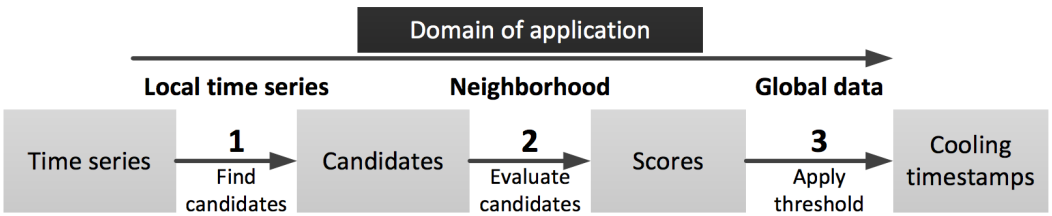

Figure 3.1: Overview of the proposed rinsing detection framework.

ure 3.1). Learning the respective parameter configuration is realized by Markov-Chain Monte Carlo sampling. The framework was optimized so that it is possible to detect rinsing events intraoperatively by minimizing delay time.

3.1.1 STREAMING RINSING DETECTOR

We observed that neurosurgeons apply cortical NaCl rinsings in very heterogeneous ways making the streaming detection of rinsing events a challenging task. In the following we will give a schematic overview to the rinsing event detector for continuous thermal measurements. A detailed discussion can be found in [11].
A rinsing event denotes the point of time after a cold NaCl solution was applied to the cortex. This event causes a characteristic pattern into sorted thermal data $s(p, i) = t_j$ of pixel p, index $i \in [1, .., n]$ and time stamp t_j. The quality of a rinsing event of pixel i is quantified by $match_i$:

$$match_i = f_{\text{norm}} \times \sum_{i=x_1}^{x_{step}} \left| T(p, s(i)) - corr(i) \right| < \text{thr}_{\text{div}} \tag{3.1}$$

given normalization factor f_{norm}, measured temperature $T(p, s(i))$ of pixel p at time index i. x_{corr} denotes a correlation function (following the shapelet idea of Ye and Keogh[24]) that is used to compute the similarity of the measured thermal signal with a single exponential function relative to the threshold thr_{div}. The chosen single exponential function can be seen as approximation to tissue heating[16].
We integrate information about detected rinsing events of adjacent pixels into the framework by

$$score(i, j) = factor(match_i, match_j) \times max(dT_i, dT_j) \tag{3.2}$$

with dT_i and dT_j being the maximum temperature differences in the analysed temporal windows of pixels i and j while $match$ represents the similarity of both cooling events. $score_{sum}(j)$ integrates the local score of pixel j over its neighbours $\mathcal{N}_j$

$$score_{sum}(j) = \sum_{i \in \mathcal{N}_j} ln(\|i - j\|_2^2 + 1)^{-1} score(i, j) \tag{3.3}$$

A rinsing event is flagged as detected iff $score_{sum}(j)$ is greater than a learnt threshold. Since several rinsings can occur during continuous thermal imaging a selection scheme is required for comparable data analysis. The basic idea is to match the rinsing event's time stamp with an estimated reference time stamp ts_{ref}

$$ts_{ref} = \underset{t_j \in \mathcal{C}}{argmax} \left\{ \sum_{i=-2}^{i=2} h(t_{j+i}) \right\} \tag{3.4}$$

which resembles the time stamp of a cooling event that affected the highest number of pixels. The detector's parameters are learnt once by an offline Metropolis-Hasting Markov Chain Monte Carlo sampler[6].

id	sex/age	pathology	result	comment
1	f/61	MCA infarct	negative	too low contrast
2	f/61	MCA+ACA infarct	negative	liquid too hot
3	m/59	MCA infarct	positive	
4	f/50	MCA infarct	questionable	classification unclear
5	f/63	vasoplastic infarct	positive	
6	f/75	MCA infarct	positive	

Table 3.1: Overview of results from classifying the decay constant of tissue heating after application of an intraoperative rinsing to the cortex.

3.1.2 TISSUE STATE CLASSIFICATION

Tissue perfusion is then approximated by Antoni Nowakowski's double exponential model[16]:

$$T(t) = T_{equ} + \Delta T_1 exp(-t\lambda_1) + \Delta T_2 exp(-t\lambda_2) \tag{3.5}$$

T_{equ} depicts the tissue's equilibrium temperature while ΔT_1 and ΔT_2 are scaling coefficients. The temperature decay constants λ_1 and λ_2 characterize the tissue's temperature change rate. At least two sources influence the tissue's heating behaviour: temperature change caused by the applied fluid and the temperature change induced by subcortical tissue and perfusion. We assume that λ_1 of the fluid is larger than λ_2 of the imaged tissue since fluid drains quite fast compared to tissue heating.
Suppose λ_2 describes the heating behaviour of underlying tissue, then we expect very characteristic values in case of ischaemic stroke. An increased perfusion or even overperfusion of tissue yields significantly increased λ_2 at respective sites. Suppose λ_2 is sampled from latent tissue state $\mathcal{S} = \{ischaemic, uncertain, healthy\}$. The expected behaviour of λ_2 is approximated by

$$\begin{aligned} \lambda_2^{ischaemic} &\sim N(\mu_i, \sigma_i) \\ \lambda_2^{uncertain} &\sim N(\mu_u, \sigma_u) \\ \lambda_2^{healthy} &\sim N(\mu_h, \sigma_h) \end{aligned}$$

$\Theta = (\mu_i, \mu_u, \mu_h, \sigma_i, \sigma_u, \sigma_h)$ are estimated by Expectation-Maximization algorithm. The 3-GMM yields $p(\lambda_2^{\mathcal{S}} = \lambda_2; \Theta)$ which denotes the probability of λ_2 belonging to any of the expected classes. This allows the following greedy segmentation strategy:

$$\widetilde{s(p)} = \underset{s \in \mathcal{S}}{argmax}\ p(\lambda_2^s = \lambda_2; \Theta) \tag{3.6}$$

Each state's probability might be a reasonable indicator to further infer knowledge regarding the progression of the ischaemic demarcation.

3.2 APPLICATION AND CONCLUSION

We applied the novel framework to several cases suffering from severe ischaemic strokes with indicated decompressive craniectomy. The infarct demarcations were further segmented in pre- and postoperative CT measurements by a neurosurgeon. A qualitative evaluation of

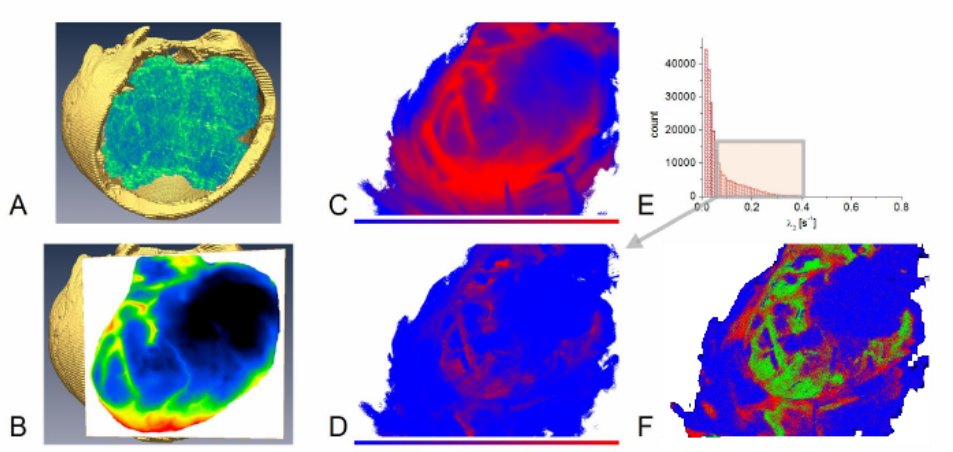

Figure 3.2: **A** the infarct demarcation is segmented as green-blue in a post-operative CT recording. Subimage **B** shows the orientation of the thermal image to the CT dataset. **C** depicts the temperature distribution at equilibrium temperature after the rinsing. **D** displays the spatial distribution of λ_2 and **E** shows the histogram of all λ_2 values. **F** represents segmentation of perfusion properties. The estimated hypoperfused tissue state (blue) correlates with postoperative infarct demarcation. Some tissue is located near well perfused arteries (green) and might indicate areas that might be affected by further ischaemic progression.

the resulting segmentations base on the categories positive, questionable and negative. Two cases yielded rejected classifications caused by erroneous cortical rinsings, which enforces the requirement for more robust cooling protocol to prevent this issue. Analysis of one dataset yielded a questionable result, meaning that more tissue was classified as healthy than the CT infarct demarcations indicate. We suspect the necessity for more fine-grained classification of uncertain tissue states being related to this issue. In three cases we found a correlation of the segmented perfusion parameters with infarct demarcations as observed in pre- and postoperative CT measurements. The developed novel rinsing detection framework grounds on optimized machine learning based detector to classify thermal characteristics of cortical rinsings with minimum delay. This detector allows us to quantify and analyse cortical perfusion (state) during cerebral infarction by a commonly used intraoperative approach even in unperfused tissue. In conjunction with preoperative CT recordings, the framework provides the surgeon valuable information regarding the progression of infarct demarcations. Latter might be used a building block for research of future local intraoperative therapies.

4 PENALIZED REGRESSION SPLINES FOR INTRAOPERATIVE FUNCTIONAL THERMOGRAPHY

Functional imaging is a common and important task in neuroscience. Commonly used mathematical frameworks like SPM[5] allow the integration of arbitrary experimental conditions into a linear model and provide statistical inference methods to infer significant responses to these conditions. Our model extends this idea by integrating piecewise-linear characteristic noise patterns and time-behaviour of thermal imaging, which would otherwise prevent reliable statistical inference on intraoperative thermal imaging data.

4.1 SEMIPARAMETRIC MODELLING OF EVOKED NEURAL ACTIVITY

In order to minimize post-operative functional deficits we propose to visualize neural activity by intraoperative thermal imaging[13]. This grounds on the fact that neural activity induces a neurovascular coupling chain, leading to an increase of regional cerebral blood flow (rCBF) at functionally active sites. This change in rCBF also correlates with small temperature changes, that can be measured by high-sensitive thermal imaging devices. We now extend prior findings of Gorbach et al.[7] by a sound semiparametric model (see [18] for an introduction to semiparametric regression) for thermographic data. The proposed semiparametric model consists of experimental and random effects. The random effects map both high-frequent behaviour like periodic motion and other artefacts and low frequent non-linear temporal drift behaviour.
FMRI experiments have shown that neural activity initiates the neurovascular coupling chain. Latter also induces deviating thermal behaviour into thermal time courses caused by altered regional perfusion. This is typically propagated through several tissue layers, for what reason we expect the thermal signal to resemble a smooth bell-like curve. We propose to approximate this curve by a Gaussian function with μ resembling the time-to-peak and σ being its width:

$$\frac{1}{\sigma\sqrt{2\pi}} exp((-(t_i - \mu)/2\sigma)^2) \tag{4.1}$$

The semiparametric model consists of two random effects with both resting upon B-Spline

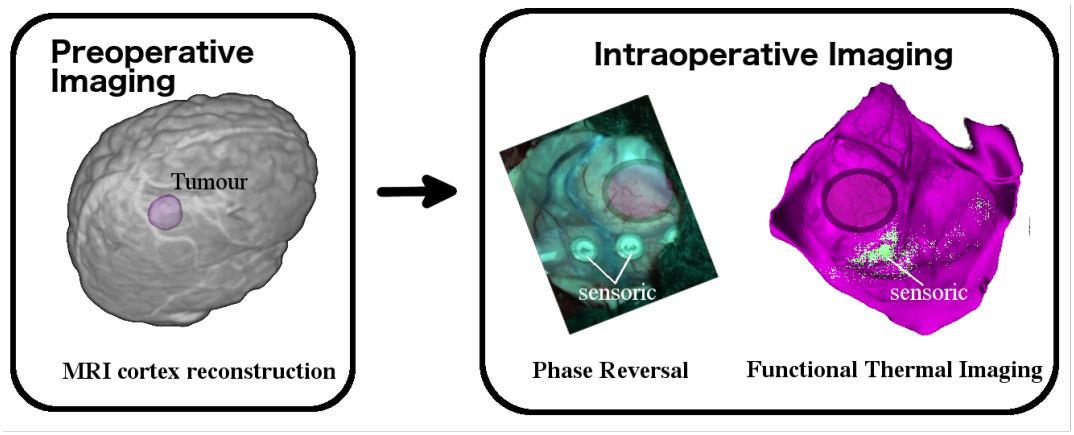

Figure 4.1: The left image shows the 3d cortex reconstruction from a preoperative MRI dataset. The tumour is demarcated in purple color. Analysing thermal imaging data by our novel semiparametric regression framework now allows to unveil sensoric activity at fine-grain resolution compared to prevalent phase reversal.

basis functions. The first random component consists of less knots to approximate the low-frequent temporal drift. The second random component approximates unwanted high--frequent behaviour. Both are modelled as degree k B-Spline by $Z_j = B_{\bullet,k}$ ($j \in \{1, 2\}$, see [3] for details) and the experimental conditions are modelled as of equation 4.1 (depending on the actual experimental protocol) and plugged into X. All of them are stacked into $G = [X, Z_1, Z_2]$. In order to prevent the second component to account for low-frequent patterns and by this hiding the experimental conditions, we add an additional frequency penalty to the respective model formulation:

$$\min_b ||Gb - y||_2^2 + \lambda ||PWGSb||_2^2 \tag{4.2}$$

given the wavelet transformation matrix W and the signal estimate Gb containing fixed and random effects.

$$S = blkdiag(0_{\text{noFixedEffects}}, 1_{\text{noRandomEffects}}) \tag{4.3}$$

$$P = blkdiag(I_{128}, 0_{m-128}) \tag{4.4}$$

Finally, P and S restrict the penalty to lower wavelet scales (dyad 1 through 6) of the random effects to decrease the low-energy power of the respective estimate. This model can be solved analytically by the penalized normal equations

$$\widehat{b}(\lambda) = (G^T G + \lambda S^T G^T W^T P^T PWGS)^{-1} G^T y \tag{4.5}$$

The non-uniformity correction of thermal imaging system introduces regular discontinuity points into the data. To account for this issue, we estimate the temporal position t_js of each non-uniformity correction event and add an additional B-Spline knot at each t_j to the high-frequent B-Spline model. This approach introduces additional flexibility into the model since it is possible to account for steep changes at respective time points.
Finally, hypothesis testing at Bonferroni corrected level α_{bonf} is employed to unveil statistically significant parameter estimates of the experimental conditions (see figure 4.1) that correlate with evoked neural activity.

Table 4.1: Results of intaoperative SSEP analysis.

case	sex / age	pathology	location	preop. clinical condition	activation TI	IOI
1	m / 58	metastasis adeno-ca.	precentral l.	hemiparesis r. (4/5)	positive	correlation
2	f / 33	metastasis mamma-ca.	parietal l.	facioplegia	positive	no OI
3	m / 79	metastasis melanoma	frontoparietal r.	hemiparesis l. arm (3/5) l. leg (4/5)	positive	correlation
4	f / 72	glioblastoma	parietal r.	hemiparesis l. leg (3/5)	weak	weak correlation
5	m / 69	glioblastoma	parietooccipital l.	symptomatic seizures	positive	correlation
6	m / 72	astrocytoma grade III	parietal l.	hemiparesis brachiofacial	none	weak signal
7	f / 60	metastasis RCC	parietal l.	no paresis	weak	no OI
8	f / 70	glioblastoma	parietal l.	hypesthesia 4th and 5th finger r.	none	strong signal
9	f / 84	anaplastic meningioma	frontoparietal l.	progressing half-side-disability	positive	no OI

4.2 RESULTS

The cohort consists of data recorded during tumour resection near somatosensory cortex. The patients were under general anaesthesia and focal activations were provoked by contralateral median nerve stimulation. The stimulation protocol consisted of 10 repeated 30 *s* stimulation and 30 *s* rest phases. Besides statistical analysis of thermal imaging data further validation was accomplished by concurrent optical imaging measurements allowing a qualitative comparison of the achieved results, by electrophysiological measurements (phase reversal) and anatomic localization of the estimated eloquent areas. We expect the accuracy of optical imaging to be better than thermal imaging since the method provides increased penetration depth compared to thermal imaging yet at cost of being sensitive to light scattering and reflection. In all cases we validated the occurrence of sensory activity on the exposed cortex by intraoperative phase reversal. The results of the proposed semiparametric regression framework are shown in table 4.1. Positive denotes a recovered clear delimited statistically significant activation in thermal imaging (as shown in figure 4.1) and intraoperative optical imaging, whereas the focal activation centres correlated in both modalities. By weak we denote results with sparse clusters of active pixels whose spatial position correlates with optical imaging. Weak and positive classified results were further validated by their anatomic localization meaning that this label is only preserved if the found eloquent site corresponds to the expected site being responsible for contralateral stimulations of median nerve. Negative means inconsistent results with thermal imaging rejecting activity while optical imaging found activity. The only two negative results were caused by a suboptimal (skewed) orientation of thermal camera while the cortex showed strong convexity and Gyrus postcentralis being located at the boundary of the trepanation. All these suboptimal measurement conditions degrade the overall accuracy and therefore prevent the detection of weak signals.
We were able to successfully unveil statistically significant somatosensory activity by a new semiparametric regression framework that incorporates experimental conditions as well as artefacts of thermal imaging systems. The model further enables the scientists to adopt the experimental conditions to arbitrary stimulation protocols, so that the application domain is not limited to the analysis of the primary somatosensory cortex. The surgeons gets a tool to unveil and visualize cortical activity intraoperatively which in case of tumour resections near eloquent areas supports the neurosurgical decision in terms of potential postoperative functional loss or limitations.

5 SUMMARY

Neurosurgery is a highly specialized and technologically demanding branch of surgery for treatment of disorders of the central nervous system. In this work, we discuss methods to improving the predictive accuracy of intraoperative thermal neuroimaging as well as provide mathematical frameworks to analyse two specific pathologies intraoperatively: brain tumours and ischaemic strokes. For this purpose we discussed necessary extensions to establish thermal imaging as flexible and robust neurosurgical decision support system. Camera movement artefacts are filtered by principal component analysis in time-frequency domain. We further extended this approach by a realtime optical flow-based motion correction scheme running on FPGA hardware. In order to correlate characteristic objects and functional information of preoperative volumetric scans (like MRI) with results of intraoperative 2D imaging, we developed a multimodal image registration and image fusion framework. One application was demonstrated by integrating intraoperative thermal imaging into preoperative 3D MRI scans at mean accuracy of 2.46mm.

In case of acute ischaemic strokes intraoperative analysis of cortical perfusion provides information regarding the progression of infarct demarcations. In combination with the analysis of tissue composition these information might be used to isolate hypoperfused tissue that might be subject to future local intraoperative therapies to preserver or even recover functionality. This long-term goal might decrease potential post-operative functional defects. For this purpose we developed a machine learning framework for online detection of intraoperative cortical NaCl rinsings. Latter induce a temperature gradient to cortical tissue which is propagated into deeper tissue layers. After rinsing event classification, tissue heating is modelled and quantitatively analysed to recover standardized perfusion parameters. In case of patients suffering ischaemic strokes the results indicate that the temperature decay time of heating processes allow to draw conclusions about tissue's perfusion state. We showed that these temperature decay constants correlate with the infarct demarcation as seen in post-operative CT measurements of the same patient. Integrating this information with knowledge from preoperative CT imaging the surgeon might yield valuable information regarding the progression of infarct demarcations. Latter might be a building block for research of future local intraoperative therapies.

Tumour resections require the differentiation of functional from pathological tissue to preserve the patient's postoperative quality of living as long as possible. Somatosensory evoked potentials (SSEP) are a common method to provoke neural activity on primary somatosensory cortex. Neural activity also causes weak changes in cortical perfusion that correlate with

temperature changes in the emitted cortical heat. We analyse these temperature changes by an advanced semiparametric regression framework that combines deterministic experimental SSEP conditions and random components describing low- and high-frequent background signals. The promising results were validated by concurrently acquired intraoperative optical imaging data. Latter approach was only possible through our advanced hardware setup. To the best of our knowledge, we are first to realize concurrent optical and thermal imaging. Generally speaking the developed regression framework allows to incorporate arbitrary experimental setups for the evocation of neural activity. The visualization of neural activity during neurosurgical tumour resections allows to guide medical decisions regarding the extent of tumour mass removal. Postoperative functional limitations or deficits significantly affect the patient's outcome for what reason tissue resections require robust intraoperative schemes for the visualization of eloquent areas.

The methodical achievements of this thesis improve the predictive accuracy of thermal imaging and hence allow demanding applications. Motion correction and multimodal image fusion depict important building blocks of medical decision support systems. The proposed semiparametric regression framework was employed for monitoring of somatosensory activity. The generic approach allows the integration of arbitrary intraoperative electrical stimulation protocols. Future applications are the visualization of neural activity of the motor cortex, visual cortex as well as during language processing tasks. Furthermore, the discussed approach to quantify cortical perfusion yields a standardized representation of vascular processes. We expect that optimized rinsing protocols might allow fine-grain differentiation of brain tissue in the future. Some experiments in case of tumour detection were already done and underline this potential future direction. The application of distributed optimization schemes for parameter estimation of the proposed semiparametric framework and for complex Bioheat equations might be potential vectors for intraoperative thermal neuroimaging.

BIBLIOGRAPHY

[1] Y. Bengio and P. Lamblin. Greedy layer-wise training of deep networks. *Advances in Neural Information Processing Systems 19 (NIPS'2006)*, (1):153–160, 2007.

[2] R. Braunschweig, J. Müller, J. Müller, and R. Tetzlaff. Nero mastering 300k cnn cells. In *European Conference on Circuit Theory and Design*, pages 1–4, 2013.

[3] C. DeBoor. *A practical guide to splines*. Springer-Verlag, New York, 1st edition, 1978.

[4] P. H. Eilers, I. D. Currie, and M. Durban. Fast and compact smoothing on large multidimensional grids. *Computational Statistics & Data Analysis*, 50(1):61–76, Jan. 2006.

[5] K. J. Friston, J. T. Ashburner, S. Kiebel, T. E. Nichols, and W. D. Penny. *Statistical Parametric Mapping: The Analysis of Functional Brain Images*. Academic Press, 1st edition, 2007.

[6] W. Gilks, S. Richardson, and D. Spiegelhalter, editors. *Markov Chain Monte Carlo in Practice*. Chapman & Hall, London, 1st edition, 1996.

[7] A. M. Gorbach, J. D. Heiss, L. Kopylev, and E. H. Oldfield. Intraoperative infrared imaging of brain tumors. *Journal of Neurosurgery*, 101(6):960–969, 2004. doi: 10.3171/jns.2004.101.6.0960.

[8] P. U. Heuschmann, O. Busse, M. Wagner, M. Endres, A. Villringer, J. Röther, P. L. Kolominsky-Rabas, and K. Berger. Schlaganfallhäufigkeit und versorgung von schlaganfallpatienten in deutschland. *Aktuelle Neurologie*, 2010.

[9] N. Hoffmann, J. Hollmach, C. Schnabel, Y. Radev, M. Kirsch, U. Petersohn, E. Koch, and G. Steiner. Wavelet subspace analysis of intraoperative thermal imaging for motion filtering. *Lecture Notes in Computer Science*, 8815:411 – 420, 2014.

[10] N. Hoffmann, Y. Radev, J. Hollmach, C. Schnabel, M. Kirsch, G. Schackert, U. Petersohn, E. Koch, and G. Steiner. Gaussian mixture models for classification of perfused blood vessels in intraoperative thermography. *Biomedical Engineering / Biomedizinische Technik*, 59:596 – 599, 2014.

[11] N. Hoffmann, G. Drache, Y. Radev, G. Schackert, U. Petersohn, E. Koch, G. Steiner, and M. Kirsch. Quantification and classification of cortical perfusion during ischemic strokes by intraoperative thermal imaging. Submitted to Journal of Biomedical Optics, 2016.

[12] N. Hoffmann, E. Koch, G. Steiner, U. Petersohn, and M. Kirsch. Learning thermal process representations for intraoperative classification of cerebral cortex. Submitted to 19th International Conference on Medical Image Computing and Computer Assisted Intervention, 2016.

[13] N. Hoffmann, Y. Radev, T. Meyer, C. Schnabel, G. Schackert, S. B. Sobottka, E. Koch, U. Petersohn, M. Kirsch, and G. Steiner. Intraoperative somatosensory activity monitoring by semiparametric analysis of thermal neuroimaging. Submitted to Journal of Biomedical Engineering / Biomedizinische Technik, 2016.

[14] N. Hoffmann, F. Weidner, P. Urban, T. Meyer, C. Schnabel, U. Petersohn, E. Koch, S. Gumhold, G. Steiner, and M. Kirsch. Generic framework for 2d-3d image fusion of thermal neuroimaging with preoperative mri. Submitted to Journal of Biomedical Engineering / Biomedizinische Technik, 2016.

[15] P. Kaatsch, C. Spix, S. Hentschel, A. Katalinic, S. Luttmann, C. Stegmaier, S. Caspritz, J. Cernaj, A. Ernst, J. Folkerts, J. Hansmann, K. Kranzhöfer, E. Kriegho-Henning, B. Kunz, A. Penzkofer, K. Treml, K. Wittenberg, N. Baras, B. Barnes, J. Bertz, N. Buttmann-Schweiger, S. Dahm, M. Franke, J. Haberland, K. Kraywinkel, A. Wienecke, and U. Wolf. Krebs in deutschland 2009/2010. häufigkeiten und trends. *Beiträge zur Gesundheitsberichterstattung des Bundes*, 2013.

[16] A. Nowakowski. *Quantitative Active Dynamic Thermal IR-Imaging and Thermal Tomography in Medical Diagnostics*, pages 1–30. CRC Press, 2016/01/17 2012. doi: doi:10.1201/b12938-8.

[17] K. Poeck. *Neurologie*. Springer-Lehrbuch, Berlin Heidelberg, 8th edition, 1993.

[18] D. Ruppert, M. P. Wand, and R. J. Carroll. *Semiparametric Regression*. Cambridge University Press, New York, 1st edition, 2003.

[19] V. Senger, N. Hoffmann, J. Müller, J. Hollmach, C. Schnabel, Y. Radev, J. Müller, M. Kirsch, U. Petersohn, G. Steiner, E. Koch, and R. Tetzlaff. Motion correction of thermographic images in neurosurgery: Performance comparison. In *Biomedical Circuits and Systems Conference (BioCAS)*, pages 121 – 124, 2014.

[20] V. Senger, R. Tetzlaff, J. Müller, N. Hoffmann, J. Hollmach, C. Schnabel, Y. Radev, M. Kirsch, U. Petersohn, G. Steiner, and E. Koch. Motion correction of thermographic images in neurosurgery. In *Proceedings of 22nd European conference on circuit theory and design*, 2015.

[21] G. Steiner, S. B. Sobottka, E. Koch, G. Schackert, and M. Kirsch. Intraoperative imaging of cortical cerebral perfusion by time-resolved thermography and multivariate data analysis. *Journal of Biomedical Optics*, 16:16001–16006, 2011. doi: 10.1117/1.3528011.

[22] P. Vincent, H. Larochelle, I. Lajoie, Y. Bengio, and P.-A. Manzagol. Stacked Denoising Autoencoders: Learning Useful Representations in a Deep Network with a Local Denoising Criterion. *Journal of Machine Learning Research*, 11(3):3371–3408, 2010.

[23] F. Weidner, N. Hoffmann, Y. Radev, J. Hollmach, C. Schnabel, M. Kirsch, G. Schackert, U. Petersohn, E. Koch, and G. Steiner. Entwicklung eines gehirn-phantoms zur perfusions- und brain shift simulation. In A. Förster, J. Füssel, M. Gelinsky, E. Koch, H. Malberg, and W. Vonau, editors, *Reports on Biomedical Engineering - Band 2: 5. Dresdner Medizintechnik-Symposium*, pages 111 – 113, 2014.

[24] L. Ye and E. Keogh. Time series shapelets: A new primitive for data mining. In *Proceedings of the 15th ACM SIGKDD international conference on Knowledge discovery and data mining*, pages 947–956, 2009.